Aerodynamic modelling of a novel vertical axis wind turbine concept

Laurence Morgan[1] **and William Leithead**[1]

[1] Dept. of Electronic and Electrical Engineering, University of Strathclyde, Glasgow, G1 1XW, UnitedKingdom

E-mail: laurence.morgan@strath.ac.uk

Abstract. This paper introduces the X-Rotor, a hybrid vertical-horizontal axis turbine concept designed to lower the cost of energy in the floating offshore environment. The development of a double multiple streamtube (DMS) simulation tool is presented alongside a thorough discussion of the secondary correction factors included in the model. New corrections for streamline curvature effects applicable to an airfoil where the blade normal plane is not aligned with the rotor plane are derived.

The DMS model is successfully validated against experimental data and against higher fidelity lifting line (LLT) simulations. Strong agreement is observed between the LLT simulations and the DMS simulations for both rotor averaged and azimuthally varying outputs, indicating that the DMS simulations can be used for future control simulations.

1. Introduction

Up to 80% of the global available resource for offshore wind is located in waters deeper than 60m and is therefore considered uneconomical for fixed bottom wind turbines[1]. This had led to large academic and commercial interest in floating offshore wind turbines (FOWTs), however, the cost of energy for floating offshore wind must be reduced to encourage widespread adoption. The use of Vertical axis wind turbines (VAWTs) has been proposed as an innovative solution to reducing costs for FOWTs, as VAWTs may be more suited to the floating environment due to multiple design synergies. These include a low drive-train position favourable for floating stability, and the compliance of floating support structures damping adverse cyclic loading associated with VAWTs [2]. This has led to resurgence in MW scale VAWT research, including the Deepwind project[3], INFLOW[4], seatwirl[5], SKWID[6], and the NOVA project[7]. A good overview of the current field is given in [8].

The X-Rotor represents a two-step innovation in the design of floating offshore wind, utilising a novel VAWT configuration combined with a secondary rotor power-take-off system. The primary rotor consists of a double V configuration designed to maximise the swept area, minimise the overturning moment typically associated with V-Rotors, and provide attachment points for the secondary rotors. The secondary rotors are utilised as a power-take-off mechanism in lieu of a conventional drive-train to circumvent both the torque ripple, and the low speed/high torque drive-trains that are inherent in conventional VAWT designs. A purely demonstrative representation of the turbine is shown in figure 1. A feasibility study [9] demonstrated that the X-Rotor has potential to reduce operations and maintenance costs by up to 55% and turbine capital costs by up to 32% yielding a cost of energy saving of up to 26%.

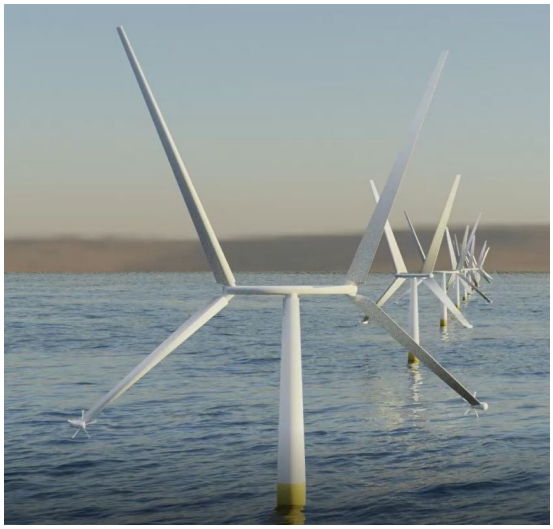

Figure 1. A non-technical rendering of the X-Rotor produced by Michael Egan.

The first step in effectively modelling the behaviour of the X-Rotor for control purposes is a fast, accurate model capable of simulating the primary rotor aerodynamics. Aerodynamic modelling of VAWTs is a less mature field than horizontal axis wind turbine (HAWT) modelling, and a number of different modelling paradigms exist including double multiple streamtube (DMS) models [10], actuator cylinder models[11] lifting line theory (LLT) models[12], panel models[13], actuator line models[14], and blade resolved CFD[7]. Whilst some cross code comparisons have shown that DMS models may not always perform accurately[15], other cross code comparisons have shown that they can effectively reproduce both rotor averaged and azimuthally varying results from higher order simulations [16], the experimental validation of DMS codes has also been largely successful [10]. Additionally, DMS models are computationally cheap, and relatively simple to implement. In this context, a bespoke DMS code has been developed at the University of Strathclyde to facilitate the simulation of vertical axis wind turbines with complex geometries and this code has been validated against experimental data and higher order simulations, the development and validation of this tool is presented in this paper.

This paper has the following structure; section 2 will provide an overview of the DMS model development, section 3 will test the validity of the model against experimental data and higher fidelity aerodynamic codes, finally section 4 will conclude the paper, outlining key findings and discussing future work.

The key novel contributions provided by this paper include; the derivation an angle of attack correction to account for streamline curvature in the case where the blade normal plane is not parallel to the rotor plane, a derivation of a conformal map to generate a virtual aerofoil that accounts for streamline curvature in the case where the blade normal plane isn't parallel to the rotor plane, the validation of a newly developed in house DMS code against lifting line theory results for a novel rotor shape using both rotor averaged and azimuthally varying quantities, and the publication of the power coefficients of the X-Rotor primary rotor.

2. DMS modelling

The DMS model was first introduced by Paraschivoiu in 1982 [17] which extended the multiple streamtube model of Strickland [18] to include two sets of actuator surfaces representing the upwind and downwind rotor halves respectively. In this implementation, 2D rotor disks are

discretised into a number of streamtubes based on the rotor azimuthal coordinate with each tube crossing a pair of actuator surfaces representing the flow's interaction with the front and back rotor half. The basic implementation of Paraschivoiu was subsequently extended to describe streamtube expansion, however the streamtubes were still considered to be parallel, allowing for discretisation by the azimuthal coordinate [10].

Read and Sharpe proposed an alternative formulation of the DMS model which intrinsically accounted for the effect of streamtube expansion and the apparent deflection of the streamlines due to fluid momentum conservation, detailed in [19].

This paper follows the formulation of Sharpe, as it considers the basis to be more physically rigorous, and utilises the variable induction approach as model accuracy beyond revolution averaged variables is considered important. Here, an overview of the DMS method is presented, followed by an introduction to the relevant secondary aerodynamic phenomena and the engineering models available to model them.

2.1. DMS overview

In order to simulate a 3D turbine through DMS, the rotor must first be discretised vertically into a number of 2D segments parallel to the plane of rotation, as shown in figure 2*a*. Each 2D segment is then discretised into a number of streamtubes with the flow conditions in each streamtube characterised by the flow in the central streamline, as shown in figure 2*b*. Each streamtube crosses two actuator surfaces representing the interaction between the upwind and downwind rotor half, as shown in figure 2*c*. The flow through each streamtube can then be calculated using momentum balance equations under the assumption that the far wake from the upstream actuator surface can be taken as the inflow condition at the downwind actuator surface.

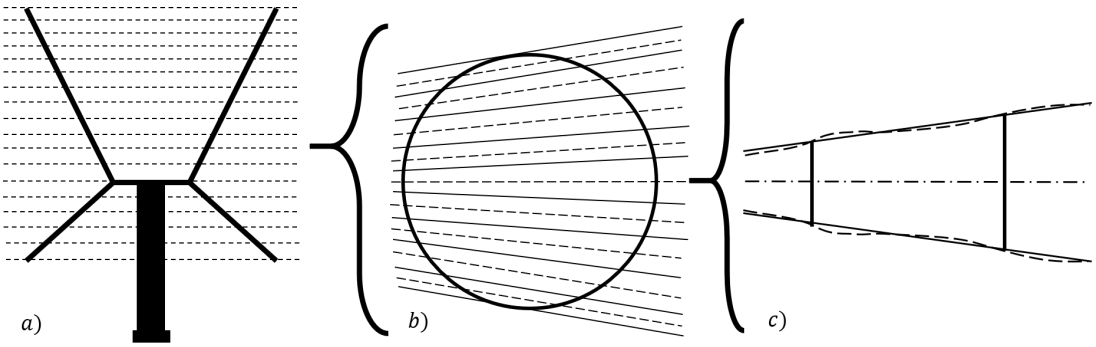

Figure 2. The discretisation procedure employed during DMS modelling.

The DMS model thus relies on the solution of momentum balance equations to resolve the local flow conditions. These are used to obtain the local blade forces which can, in turn, be integrated to obtain the rotor and blade variables of interest. This picture is complicated by the fact that the streamtube discretisation scheme cannot be completed with respect to any factor pertaining to the physical rotor geometry. This is because the location of streamtubes are not know a priori due to their dependence on the rotor loading distribution and the consequent streamtube expansion due to momentum conservation. To circumvent this issue, the rotor can be discretised by the angle subtended between the rotor radius vector and the incident streamline, henceforth referred to as the blade angle θ, rather than the angle of azimuth Θ. It should be noted that in the case of an unloaded rotor, the streamlines remain parallel and the blade angle reduces to the angle of azimuth ($\theta = \Theta$). Both θ and Θ are labeled in figure 3*a* for clarity.

The solution procedure therefore involves three steps, the determination of the flow conditions at each blade angle (as calculated through momentum balance equations), the determination of streamtube geometry (as calculated through momentum conservation), and the integration of local blade forces into relevant rotor variables. These are each discussed in the subsections below.

2.2. Local flow calculations

At each actuator surface, the flow is reduced to a one dimension problem where the retardation of the flow through an actuator surface is characterised by the induction factor, a, with

$$U_{I[u/d]} = (1 - a_{[u/d]})U_{N[u/d]} \tag{1}$$

where U_I represents the windspeed at the actuator surface, U_N represents the wind-speed at the actuator surface if the surface was not present and the subscripts $[u/d]$ are introduced to specify if variables refer to the upwind or downwind actuator surfaces. Momentum theory dictates that the thrust coefficient at each actuator surface is given by

$$C_{T[u/d]} = 4a_{[u/d]}(1 - a_{[u/d]}). \tag{2}$$

This can be equated to the thrust coefficient as calculated though the non-dimensionalised, rotation averaged forces on the blade element projected onto the streamtube's central streamline, giving

$$C_{T[u/d]} = \left[sec(\theta)\frac{Nc}{2\pi R}\right]\left[\frac{U_{a[u/d]}}{U_{N[u/d]}}\right]^2 \left[C_n(\alpha_{[u/d]})cos(\theta)cos(\eta) - C_t(\alpha_{[u/d]})sin(\theta)\right]. \tag{3}$$

The first term represents the rotation averaging, with N representing the number of blades, c representing the local chord length, and R representing the rotor radius. The second term is an artifact of the de-dimensionalisation and represents the ratio between apparent velocity at the blade element, U_a and the incident velocity at the actuator surface in the no-load scenario, U_N. The final term represents the projection of the blade element force onto the streamline, with C_n and C_t representing the normal and tangential force coefficients, α representing the angle of attack, and η representing the angle between the blade normal plane and the rotor plane. The lift, drag, normal and tangential axes, as well as the associated blade angles are shown figure 3*b*.

At the upwind actuator surface, the no-load velocity is simply given by the free stream velocity ($U_{N[u]} = U_0$) whilst at the downwind actuator surface atmospheric pressure is assumed to have recovered with the no-load velocity given by

$$U_{N[d]} = (1 - 2a_{[u]})U_0. \tag{4}$$

The apparent velocity at the blade element is given by the sum of the incident wind-speed and rotation induced velocity

$$U_{a[u/d]} = \sqrt{[\omega R + U_{I[u/d]}cos(\theta)]^2 + [U_{I[u/d]}sin(\theta)cos(\eta)]^2}. \tag{5}$$

where ω represents the rotational speed of the blade element.

Finally, the angle of attack is given as the sum of the inflow angle, ϕ and the pitch offset, β

$$\alpha_{[u/d]} = \phi_{[u/d]} + \beta = \text{atan}\left(\frac{U_{I[u/d]}sin(\theta)cos(\eta)}{\omega R + U_I[u/d]cos(\theta)}\right) + \beta. \tag{6}$$

This scheme fully describes the flow in terms of two equations with two unknowns; the induction factors $[a_u, a_d]$. The solution to any streamtube can therefore be found by equating equations 2 & 3 at the upwind actuator surface to calculate $a_{[u]}$ then at the downwind actuator surface to calculate $a_{[d]}$.

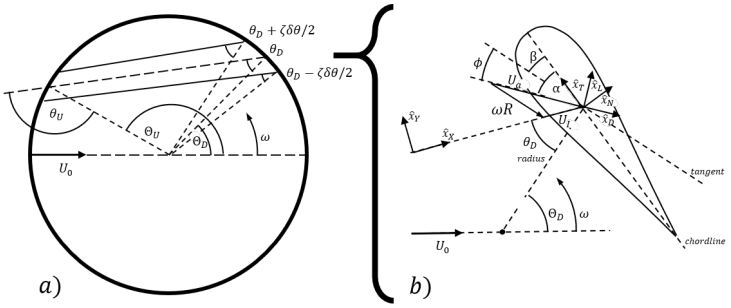

Figure 3. The streamline and blade element geometries involved in the DMS procedure.

2.3. Determination of streamtube geometry

The geometry of a single streamtube is shown in figure 3*a*, it has a central streamline which crosses the rotor at blade angles $(\theta_{[u]}, \theta_{[d]})$, and it's boundaries are given by the streamlines that pass at $(\theta_{[u]} \pm \zeta_{[u]}\delta\theta/2, \theta_{[d]} \mp \zeta_{[d]}\delta\theta/2)$.

The definition of a streamtube implies that the mass flow must be conserved which dictates that

$$U_{[u]}A_{[u]} = U_{[m]}A_{[m]} = U_{[d]}A_{[d]}, \tag{7}$$

where A represents the cross sectional area of the streamtube, and the subscript $[m]$ is introduced to represent the position at the at the mid-point between the surfaces. Assuming that the streamlines are straight within the region enclosed by the rotor segment, the area at the midpoint between the two actuator surfaces is equal to the mean streamtube area. The area of the upwind and downwind actuator surfaces can therefore be related to the mean streamtube area with

$$A_{[u]} = \left(\frac{2U_{[d]}}{U_{[u]} + U_{[d]}}\right) A_{[m]} = \underbrace{\left[\frac{2(1-2a_{[u]})(1-a_{[d]})}{(1-2a_{[u]})(1-a_{[d]}) + (1-a_{[u]})}\right]}_{\zeta_{[u]}} A_{[m]}, \tag{8}$$

$$A_{[d]} = \left(\frac{2U_{[u]}}{U_{[u]} + U_{[d]}}\right) A_{[m]} = \underbrace{\left[\frac{2(1-a_{[u]})}{(1-2a_{[u]})(1-a_{[d]}) + (1-a_U)}\right]}_{\zeta_D} A_{[m]}, \tag{9}$$

where the square bracketed terms represent the upwind and downwind expansion factors, given by ζ_U and ζ_D respectively. To facilitate the solution of the problem, it is assumed that the midpoint streamtube area is given by

$$A_{[m]} = Rcos(\theta)\delta\theta, \tag{10}$$

which is independent of streamtube loading. With this, all variables are described and the geometry of any given streamtube can be determined.

As the central streamline is not deflected, the angle of azimuth corresponding to each streamline can be calculated though integrating outward from the central streamline:

$$\Theta_{[u]}(\theta) = \pi + \int_{\pi}^{\theta_{[u]}} \zeta_{[u]}(\tilde{\theta})d\tilde{\theta} \tag{11}$$

$$\Theta_{[d]}(\theta) = \int_{0}^{\theta_{[d]}} \zeta_{[d]}(\tilde{\theta})d\tilde{\theta}. \tag{12}$$

As the expansion factor is unknown prior before the streamtube is solved, cases using a cyclic pitch regime must employ a forward estimate technique to estimate the angle of azimuth

$$\Theta^{[i+1]} = \Theta^{[i]} + \zeta^{[i]}_{[u/d]}\delta\theta. \tag{13}$$

A key impact of the proper inclusion of streamtube expansion, is that the power extraction from the tandem actuator surfaces becomes coupled through the scaling of the actuator surface area.

2.4. Resolving and Integrating Blade Forces

With the geometry determined, the flow field is fully resolved, and all that remains is the integration of blade element forces to obtain rotor/blade variables of interest. The blade torque can be obtained by numerically integrating the elemental torque contribution over the blade span

$$Q_B(\Theta) = \int_0^L \frac{1}{2}\rho U_I^2 D_Q(\Theta) dl \tag{14}$$

where the local torque contribution is given by

$$D_Q = R[C_L sin(\phi) - C_D cos(\phi)] \pm (0.25 - \xi)c[\{C_L cos(\phi) + C_D sin(\phi)\}cos(\eta)]. \tag{15}$$

Here, the $\pm$ sign refers to the upwind and downwind case respectively and ξ represents the relative attachment position of the aerofoil (measured from the leading edge). Care must be taken in the evaluation of equation 14 to ensure that the integration is taken at a specific azimuth angle rather than at a blade angle as streamtube expansion is non-uniform over the rotor height. The rotor torque is found by summing the torque contributions from each blade with an appropriate phase offset

$$Q_R(\theta) = \sum_{i=1}^{N} Q_B(\Theta + i\frac{2\pi}{N}). \tag{16}$$

With the rotor torque obtained, the power is given by the product of the rotor speed and the integral of the torque over a single rotation

$$P = \omega \int_0^{2\pi} Q_R(\Theta) d\Theta. \tag{17}$$

Blade bending moments and other rotor force coefficients can be obtained through the integration and normalisation of the appropriate force vectors.

2.5. Additional aerodynamic phenomena

In the DMS method, the aerodynamic forces on the blade sections are obtained from blade polars; look-up tables that give the forces coefficients parallel and perpendicular to the direction of the flow. These polars are typically generated for a 2D wing in steady, rectilinear flow which is not representative of the blade element conditions for a vertical axis wind turbine. Additionally, the basic DMS method does not consider the flow entering the turbulent wake state. This section will give an overview of the unique phenomena associated with VAWT aerodynamics including; Dynamic stall, tip losses, streamline curvature, and the turbulent wake state, and will provide a description of the engineering models used to characterise these phenomena.

2.5.1. Dynamic Stall Dynamic stall occurs when an aerofoils unsteady motion lead to the angle of attack exceeding the static stall angle. It is typically characterised by an increase in the lift coefficient beyond the maximum static value at angles of attack exceeding the static stall angle as flow separation is delayed, followed by a sharp increase in drag coefficient and drop in the lift coefficient as the flow separates. During reattachment, lift coefficient remains below it's static value until the flow has reattached. A thorough discussion of the phenomena can be found in [20]. The two most common engineering models used to describe this phenomena in the context of VAWTs are the Gormont model and the Leishman-Beddows (LB) model, both adapted from helicopter aerodynamics.

The Gormont model is based on reproducing the forcing behaviour using an equivalent angle of attack, calculated based on Theodorsen's theory using the non-dimensional frequency of the dynamic motion, the angle of attack relative to the static stall angle, and the gamma function, obtained as a function of aerofoil geometry, non-dimensional frequency and Mach number. Originally applied to the transonic flows experienced by helicopter blades, the model was simplified by Strickland for incompressible flow with thicker ($t/c>0.12$) aerofoils, Strickland also limited the application of the model to regions where the angle of attack is greater than the static stall angle. Paraschivoiu proposed that the model should not be applied in the rear rotor half as stall was delayed due to the high free-stream turbulence and Masse recognised that the model often over-estimated the peak lift coefficient and introduced an interpolation scheme between the static and dynamic lift coefficients. A review of the Gormont model and it's modifications can be found in [21].

In general the Gormont model is considered to be simple to apply as all but one of the required constants can be readily obtained from the static blade polar data, with Masse's interpolation constant needing to be specified. A relationship between the chord length and the interpolation coefficient was put forward by Shires [22], however it should be noted that this relationship was only loosely validated, and has not been adopted in any future works. Additionally, the angle of attack history used to calculate the non-dimensional frequency can be generated using the free-stream velocity [19], so the dynamic stall model can be implemented directly into the DMS procedure.

The LB model represents a more complete unsteady aerodynamics model, with 3 distinct sub-models describing unsteady linear attached flow described using indicial response functions and approximations of Duhamel's integral, flow separation using Kirchoff-Helmholtz theory, and vortex shedding using a series of equations based on the Mach number and a number of empirical constants. For cyclical motion, the results from LB dynamic stall models typically take 2 to 3 rotations to converge [23]. This represents a challenge with respect to DMS methods, as the induction factor calculations also rely on iterative solution methods, however the challenge is typically overcome by ignoring the unsteady calculations in the calculation of the induction factors, then using the angle of attack history from the DMS simulation to re-calculate the blade loads using the dynamic stall model, as in [24]. A further issue in the implementation of LB type DMS methods is the issue of defining the empirical constants that require unsteady data for the aerofoil at the correction Reynolds number and Mach number. Whilst a range of data is presented in [25], and methods for generating the data using CFD simulations have been proposed in [26], the requirement for these constants and their sparsity in published work represents a barrier for the models implementation.

In this paper, the Gormont model with the modifications of Strickland and Masse are used in the description of dynamic stall.

2.5.2. Tip losses The aerodynamic force on a blade can be understood to be caused by the bound vorticity on the blade, this bound vorticity leaves the blade at the blade tips in the form of tip-vorticies, generating a complex structure behind the blade. This reduces the circulation

at the blade tips, lowering the blade loads. This complex behaviour can be approximated using a tip-loss function, F. In the context of wind energy, the simplified tip loss model of Prandtl is typically invoked, using the assumption that the wake can be represented by a number of impermeable disks translated at the free-stream velocity. Numerous modifications of the tip-loss function exist for HAWTs and a thorough review is presented in [27].

With respect to VAWTs, these tip-loss functions are modified to maintain the same form of the tip-loss factor, but altering the disk spacing to better represent the vortex wake behind the rotor. The generalised form of the tip loss function is given by

$$f = \frac{2}{\pi} acos\left(exp\left[-\pi\frac{s}{d}\right]\right), \tag{18}$$

where s represents the distance from the blade tip, and d represents the distance between wake disks. Paraschivoiu proposes that the distance, d is given by

$$d = U_{w[u/d]}\frac{\pi}{N\omega}, \tag{19}$$

indicating that each of the N blades sheds a disk propagating at velocity U_W twice every rotation. Alternatively, Sharpe [19] proposed that the distance between the shed disks is given by

$$d = U_{w[u/d]}\frac{\pi R}{NU_0}. \tag{20}$$

These models are reconciled if the tip-speed ratio is equal to 1, however as the tip-speed ratio increases the tip loss function of Paraschivoiu estimates efficiency gains that are not realised in the case of Sharpe's correction.

The difference in these approaches is often masked by the normalisation scheme, applied to ensure that the tip-loss function is equal to unity (thus having no effect) at the blade center when considering H-Rotors. Paraschivoiu calculates the tip-loss contribution from the nearest blade tip, and normalises with respect to the tip-loss at the center, whilst Sharpe takes the product of both tip-loss functions, and normalised by the value of this product at the blade center. The fact that both approaches require normalisation at the blade center may imply that they may not be accurate for use in the case of V-Rotors or X-Rotors whereby the normalisation cannot occur as there is no position on the rotor blade where the tip-loss function is known to be equal to 1.

A further difference in approach can be found in how the tip-loss factor is applied. Here there are 3 options. Paraschivoiu uses the tip-loss function directly in the blade element calculations, retarding the flow velocity normal to the blade element by the calculated tip loss factor f, whilst Sharpe [19], indicates that the tip loss function should be applied such that the induction factor a, is replaced by the product af in the momentum theory calculations. In other works, such as that of [22], the approach used in HAWT BEM codes such as aerodyn[28] is applied, where the tip loss factor is applied such that

$$C_T = 4a(1-a)f. \tag{21}$$

The formulation used by Aerodyn is helpful, as it allows for Buhl's[29] correction for the turbulent wake state to be applied. The tool developed in this paper utilises the tip-loss function proposed by Sharpe, with correction applied as in equation 21.

2.5.3. Streamline curvature The effect of streamline curvature, also sometimes referred to as virtual incidence or virtual camber, describes the change in aerofoil behaviour between rectilinear and curvilinear flow. Typically, blade element polars are obtained from either wind tunnels or from simulation tools, both of which enforce rectilinear flow conditions. A blade section orbiting

a central point sees curvilinear streamlines changing the local velocity and pressure distributions around the aerofoil and introducing a virtual camber and virtual incidence effects, an early study is given in [30]. Typically, a number approaches have been used to describe this effect. Muracia derived a relative scaling factor for the lift coefficient through integrating pressures around a flat plate[31]. Loth[32] introduced an angle of attack correction, almost identical to that which was later derived by Goude [33], recently Bangga[34] derived an angle of attack correction that re-defines the angle of attack from the blade attachment position to the blade leading edge. This reproduced the virtual incidence angle, even under pitched conditions, but did not reproduce the vertical camber effects. Sharpe[19] proposed a simplification of the angle of attack correction, whereby the relationship between the normal force coefficient and the angle of attack was considered linear, and the blade was assumed to be attached at the blade center, with this a correction was applied to the normal force coefficient.

Another approach that has been beneficial both for simulation and aerofoil design is the use of conformal mapping techniques. Applying a transform that converts the curvilinear streamlines experienced by the real aerofoil, into rectilinear streamlines, onto the aerofoil itself generates a virtual aerofoil that has the characteristics of the real aerofoil in those curvilinear conditions. The aerodynamic coefficients of this virtual aerofoil can then be obtained and used in the simulation, this was first pioneered by Migliore [30]. A review of the conformal mapping techniques applied to VAWTs is given in [35]. An issue with the use of these techniques applied to V-VAWTs is that the chord to radius ratio of the rotor changes significantly along the blade due to the changing rotor radius, requiring numerous virtual aerofoils to be generated for each blade. This significantly increases the time required to simulate new rotor designs, and it was therefore chosen to apply angle of attack corrections, such as those proposed by Loth and Goude.

One issue with the currently discussed correction factor is that each of them assume that the blade normal plane is parallel to the plane of rotation, which is not the case for V-Rotors or X-Rotors. Appendix A re-derives an angle of attack correction and a conformal map that can be applied to describe the effects of streamline curvature when the blade normal plane is not aligned with the plane of rotation. The angle of attack correction used by the tool developed in this paper is given by

$$\alpha' = \alpha + cos(\eta) \left\{ \frac{1}{4}\frac{c}{R} + \frac{1}{2}\frac{(1-2\xi)c}{R} \right\}. \tag{22}$$

2.5.4. Turbulent wake state Experimentally, the parabolic relationship between induction factor and rotor thrust provided in equation 2 has been found to break down for induction values around (a >0.4) after which an approximately linear relationship emerges[28]. It is understood that this occurs because the wake behind the rotor disk enters a turbulent state and the relationship derived using actuator disk theory (based on Bernoulli's equation) breaks down. The classic correction applied in this state is obtained by taking a linear extrapolation of the thrust parabola, however this becomes problematic when a tip loss correction is applied to the thrust coefficient, leading to a discontinuity at the point of transition which can interfere with the iterative solution process. Bhul [29] proposed replacing the linear interpolation with a second order polynomial, which transitions smoothly from the momentum parabola to the maximum value at ($a = 1$). The value of the two endpoints, and the smoothness condition provide the 3 boundary conditions required to calculate the momentum coefficient.

A new development in actuator modelling in general was introduced by Ayati[36] who utilised an extension of Rankie-Froude momentum theory proposed by Sterios and Hultmark which is valid for a much wide range of loading, and doesn't predict wake reversal for highly loaded situations. This approach seems very promising for the application of DMS at higher tip-speed ratios where the rotor loading is generally above the range at which Rankie-Froude momentum

theory is applicable.

The tool developed in this paper utilises the correction factor proposed by Bhul.

3. Model Validation

3.1. Validation against experimental data

Data from the Sandia 17m experimental wind turbine is chosen to validate the DMS model as the turbine was well instrumented, with blade force coefficients available [37] as well as the rotor power curve[38]. Additionally, because the rotor model is strutless, the uncertainties around the modelling of secondary rotor structures are minimised. The rotor was a 2 bladed straight-arc-straight Darrieus shape with a radius of 8.36m and a height to diameter ratio of 1 leading to a swept area of 187.1m^2. Each blade has a constant chord length of 0.61m with a NACA0015 section[38].

Figure 4 shows the experimentally determined rotor power curve against the output from the DMS model. In this case all of the previously described correction factors are active apart from the tip loss correction (as the rotor has no well defined blade tips). The agreement between the DMS model the experimental data in the area close to rated power is clear, and both the magnitude and location of the maximum power coefficient is well defined. At high tip-speed ratios the DMS model over predicts the available power, this may be because of an underestimation of the minimum drag coefficient of the blade at high tip-speed ratios. At very low tip-speed ratios, the model over predicts the power coefficient, this is due to the dynamic stall model over-estimating increase in the blade force associated with vortex lift.

Figures 5 & 6 show the normal and tangential force coefficients take at the equatorial rotor position for a low tip speed ratio ($\lambda = 2.39$) and an intermediate tip speed ratio ($\lambda = 4.6$) respectively. An initial observation is that the DMS model captures the experimental data relatively well. However, at the low tip speed ratio, it is clear that the dynamic stall model becomes active at an azimuthal angle of around 130° and causes an over-estimation in both the tangential and normal force coefficients after that point. A sharp drop in the tangential force coefficient is also erroneously predicted at 190° due to the model predicting a prolonged period before the flow has re-attached. In the intermediate tip speed ratio case, the force coefficients are relatively well described.

3.2. Validation against higher order simulation codes

Here, higher fidelity numerical simulations of the X-rotor are completed using the LLT codes CACTUS[39] and QBlade[12] and compared to the DMS model. The X-Rotor geometry is described in table 1. It should be noted that all values given at the blade and root tips can be interpolated linearly to obtain the span-wise distribution.

Initially, the LLT are are run without secondary corrections. As the models intrinsically account for the effects of the tip loss and the turbulent wake state, these are compared to a base DMS code which includes tip-loss corrections and the turbulent wake state. This examines how well models can reproduce each others behaviour in their most basic form, isolated from the differences cause by different dynamic stall and streamline curvature models. Subsequently, the CACTUS code is run with corrections for both streamline curvature, and a Leishman-Beddowes dynamic stall model and compared to the fully corrected DMS simulations.

Figures 7 & 8 show the comparison of the base model power curves and the corrected power curves. The general shape of the curve is well captured, and the tip speed ratio corresponding to the maximum power coefficient is in agreement between the 3 models. The DMS model over predicts the peak power coefficient relative to the other two models, however the relative uncertainty in the two LLT model outputs is of similar magnitude to the uncertainty between the DMS method and the CACTUS model. Comparing fully corrected DMS against CACTUS, there is considerable agreement in the low tip-speed ratio range, despite the fact that they use

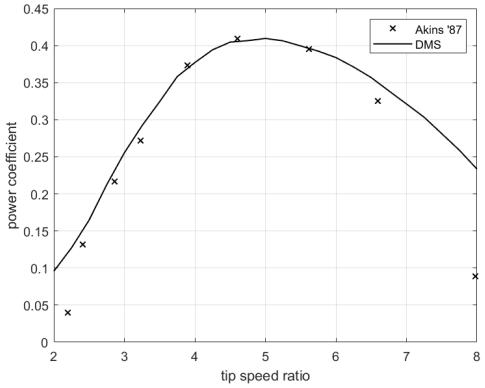

Figure 4. Power coefficient from the DMS model compared to the Sandia 17m demonstration turbine.

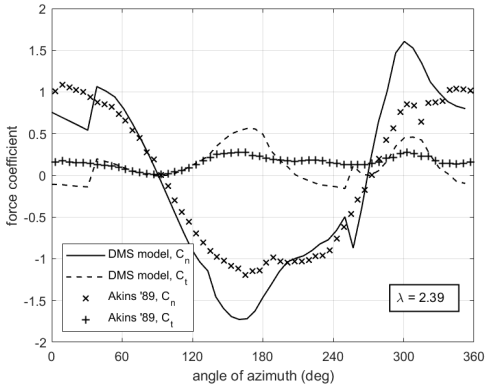

Figure 5. Normal and tangential force coefficients from the DMS model compared to the Sandia 17m demonstration turbine for $\lambda = 2.39$.

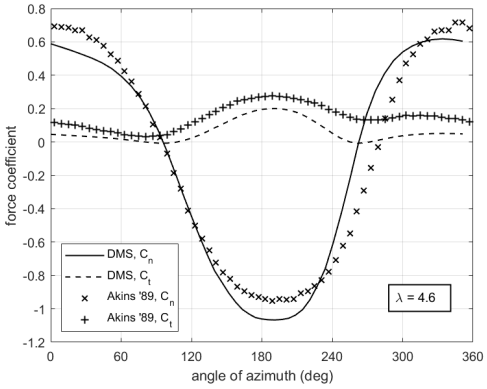

Figure 6. Normal and tangential force coefficients from the DMS model compared to the Sandia 17m demonstration turbine for $\lambda = 4.6$.

Table 1. X-Rotor Primary Rotor configuration.

Blade	R_{root}[m]	R_{tip}[m]	η [deg]	$\beta[deg]$	$c_{root}[m]$	$c_{tip}[m]$	Root section	Tip section
Upper	25	75	30	0	10	5	NACA0025	NACA0008
Lower	25	75	50	0	14	7	NACA0025	NACA0008

different dynamic stall models. The location and magnitude of the maximum power coefficient show good agreement, with the DMS model predicting a maximum power coefficient of 0.46 at a tip speed ratio of 4.25, whilst CACTUS predicts a maximum power coefficient of 0.47 and a tip speed ratio of 4.5. As the tip speed ratio increases further, the DMS model predicts a more rapid tailing off of the power coefficient compared to the LLT model. From the good agreement shown between both the base and fully corrected models, it is considered that the DMS model is able to produce power coefficient curves that are in agreement with higher fidelity lifting line codes.

Figures 9 & 10 show the torque coefficient obtained from the un-corrected models at a low tip speed ratio of $\lambda = 2$ and an intermediate tip speed ratio of $\lambda = 4.5$. There is strong agreement between the DMS method and the two LLT models for both tip-speed ratios, and the DMS method captures both the 4 peak torque spectrum at the low tip speed ratios, and the 2 peak torque spectrum at intermediate tip speed ratios. The amplitude of the torque coefficient is also well reproduced by the DMS model. Figures 11 & 12 show the torque coefficient obtained from the fully corrected models at a low tip speed ratio of $\lambda = 2$ and an intermediate tip speed ratio of $\lambda = 4.5$. Again, the agreement between the models is clear. At low tip-speed ratios, the shape of the torque curve is well described, however the peak torque coefficients are overestimated due to the difference in dynamic stall models. At intermediate tip-speed ratios, the torque coefficient curves and peak torque coefficients show good agreement. From this strong agreement, it can be inferred that the DMS model can accurately reproduce the torque profile as calculated using the higher order LLT simulation method, and can be used in future investigations into the behaviour of the X-Rotor.

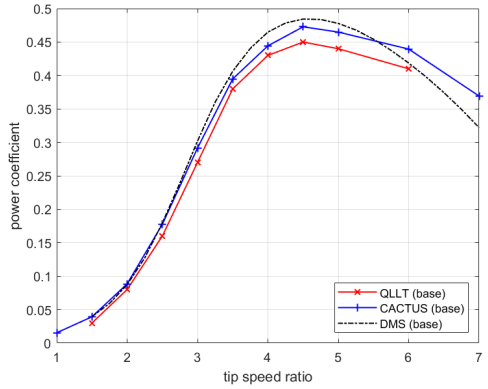

Figure 7. X-Rotor power curve without corrections

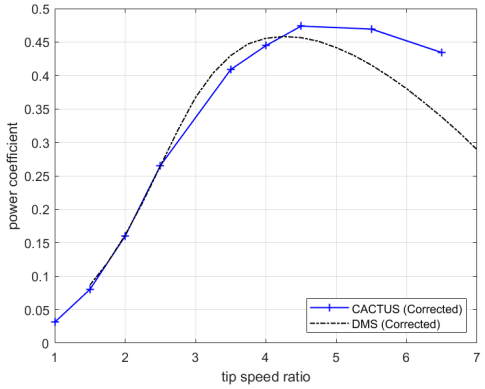

Figure 8. X-Rotor power curve with corrections

4. Conclusions and future work

This paper has described the development and validation of a fast and accurate DMS model for the goal of simulating the X-Rotor primary rotor. The underlying physics of the DMS method is rigorously introduced, and a thorough review of the secondary correction factors is introduced. The model is validated against both experimental data and higher fidelity simulation codes. The ability of the model to describe both rotor averaged and azimuthally varying values to a high degree of accuracy is demonstrated. Additionally, a derivation of flow curvature corrections in the case where the blade normal plane is not parallel to the rotor plane is provided in appendix A1 which, to the authors knowledge, has not been shown elsewhere.

With a simulation tool capable of accurately describing the X-rotor primary rotor aerodynamics, work is now ongoing into integrating this model into a wider control model that includes the secondary rotor aerodynamics and the structural and electrical dynamics of the system. Additionally, work is ongoing on the further validation of the DMS model.

5. Acknowledgements

The authors would like to acknowledge the EU H2020 XROTOR Project 101007135 and the EP/S023801/1 EPSRC Centre for Doctoral Training in Wind and Marine Energy Systems and Structures for funding this research.

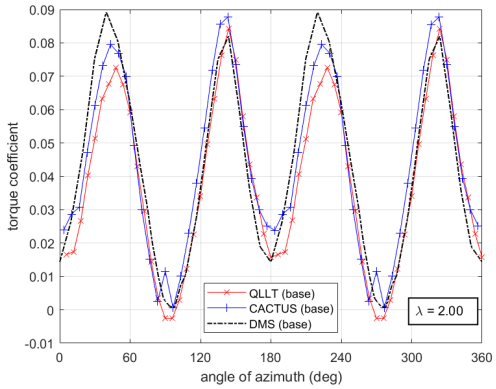

Figure 9. X-Rotor torque coefficient for $\lambda = 2$ without corrections.

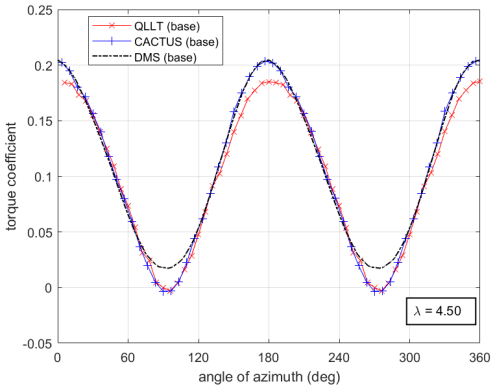

Figure 10. X-Rotor torque coefficient for $\lambda = 4.5$ without corrections.

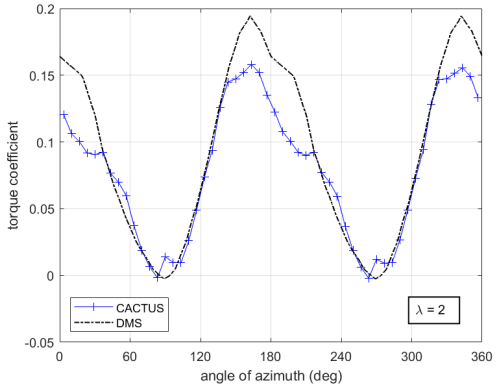

Figure 11. X-Rotor torque coefficient for $\lambda = 2$ with corrections.

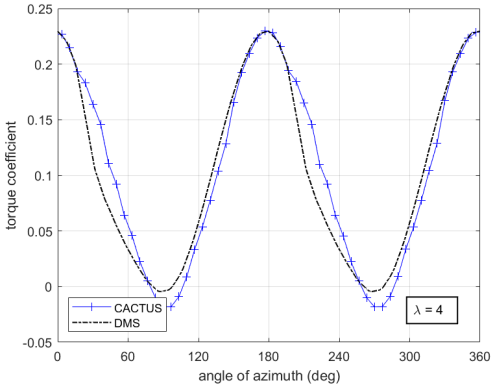

Figure 12. X-Rotor torque coefficient for $\lambda = 4.5$ with corrections.

References

[1] Wind Europe 2018 *Floating offshore wind energy a policy blueprint for Europe*
[2] Sutherland H J, Berg D E, and Ashwill T D 2012 *Technical Report for Sandia Nat. Labs.* SAND2012-0304
[3] Paulsen U S, Borg M, Madsen H A., Pedersen T F, Hattel J, Ritchie E, Ferreira C S., Svendsen H, Berthelsen P A, Smadja C 2015. *Energy Procedia* **80** 329-41
[4] INFLOW–Industrialization Setup of a Floating Offshore Wind Turbine *accessed 20/02/2022* Available online: *https://cordis.europa.eu/project/id/296043.*
[5] SeaTwirl *accessed 20/02/2022* Available online: *https://seatwirl.com/.*
[6] MODEC 2013 *Floating Wind & Current Hybrid Power Generation: Savonius Keel & Wind Turbine Darrieus* Product Brochure Tokyo
[7] Wang L, Kolios A, Delafin P L, Nishino T and Bird T 2015 *European Wind Energy Association Annual Conference and Exhibition 2015* Paris EWEA
[8] Hand B and Cashman A 2020 Sustainable Energy Technologies and Assessments **38** 100646.
[9] Leithead W et al 2019 J. Phys.: Conf. Ser.**1356** 012031
[10] Paraschivoiu I. 2002 *Wind Turbine Design: With Emphasis on Darrieus Concept* Presses Inter Polytechnique
[11] Madsen H Aa et al 2014 J. Phys.: Conf. Ser.**555** 012065
[12] Marten D, Pechlivanoglou G, Navid Nayeri C, and Oliver Paschereit C 2018. Journal of Fluids Engineering, **140** 021107
[13] Zanon A, Giannattasio P and Simão Ferreira C J, 2013 Wind Energy **16(5)** 661-80
[14] Mendoza V, Bachant P, Ferreira C, and Goude A. 2019 Wind Energy **22(2)** 171-88
[15] Ferreira C S, Madsen H A, Barone M, Roscher B, Deglaire P and Arduin I 2014 J. Phys.: Conf. Ser.**524** 012125
[16] Delafin P L, Nishino T, Kolios A and Wang L 2017 Renewable Energy **109** 564–75
[17] Paraschivoiu I. 1981 NASA. Lewis Research Center Wind Turbine Dyn
[18] Strickland J 1975 *Technical Report for Sandia Nat. Labs.* SAND-75-0431
[19] Freris L 1990 Wind energy conversion systems New York Prentice Hall
[20] Leishman G J, 2006 Principles of helicopter aerodynamics Cambridge Cambridge university press
[21] Masson C, Leclerc C, and Paraschivoiu I 1998 International Journal of Rotating Machinery **4(2)** 129–139
[22] Shires A. 2013 Energies **6(5)** 2501–2520
[23] Dyachuk E and Goude A 2015 Energies **8(2)**1353-72
[24] Wang K, Hansen M O L, and Moan T 2015 Wind Energy **18(1)** 91–110
[25] Dyachuk E, Goude A and Bernhoff H 2014 AIAA journal, **52(1)** 72-81.
[26] Hand B, Kelly G and Cashman A. 2021 Journal of Solar Energy Engineering **143(4)**: 044501
[27] Branlard E. 2011. Wind turbine tip-loss corrections: Review, implementation and investigation of new models *Masters Thesis* Risø DTU
[28] Moriarty P J and Hansen A C 2005 AeroDyn Theory Manual NREL NREL/TP-500-36881
[29] Buhl Jr M L 2005 A New Empirical Relationship between Thrust Coefficient and Induction Factor for the Turbulent Windmill State *Technical Report* NREL/TP-500-36834
[30] Migliore P and Wolfe W. 1979 17th Aerospace Sciences Meeting New Orleans 112
[31] Muraca R J, Stephens M V and Dagenhart R J 1975 Theoretical Performance of Cross-Wind Axis Turbines with Results for a Catenary Vertical Axis Configuration *NASA Technical Memorandum* NASA TM X-72662
[32] Loth J L and McCoy H. 1983 Journal of Energy, **7(4)** 313–8
[33] Goude A 2012 Fluid Mechanics of Vertical Axis Turbines *PhD Thesis* Uppsala university
[34] Bangga G, Dessoky A, Lutz T, and Krämer E. 2019 Energy **182** 673–88
[35] van der Horst S, van de Wiel J, Ferreira C S and García N R 2016. 34th Wind Energy Symposium San Diego California
[36] Ayati A A, Steiros K, Miller A M, Duvvuri S and Hultmark M 2019 Wind Energy Science, **4(4)**, 653–62
[37] Akins R E 1989 *Technical Report for Sandia Nat. Labs.* SAND-89-7051
[38] Akins R E, Berg D E, Cyrus W T 1987 *Technical Report for Sandia Nat. Labs.* SAND-86-2164
[39] Murray J and Barone M 2011 49th AIAA Aerospace Sciences Meeting, Orlando, Florida

Appendix A. Derivation of curvature correction model for V-Rotors.

Appendix A.1. Dynamics

The velocity at an arbitrary point on the surface of an aerofoil rotating around a central axis with the blade normal plane at an angle η to the rotational plane, as shown in figure A1a, is given by

$$\begin{bmatrix} U_x \\ U_y \end{bmatrix} = \omega \begin{bmatrix} R + ycos(\eta) \\ -xcos(\eta) \end{bmatrix} + U_0 \begin{bmatrix} sin(\theta) \\ cos(\theta)cos(\eta) \end{bmatrix} \tag{A.1}$$

the x, y axis with 0 at the blade attachment point as in figure A1b . In the case of a pitching aerofoil in rectilinear flow, shown in figure A1c, we have

$$\begin{bmatrix} U_x \\ U_y \end{bmatrix} = \tilde{\omega} \begin{bmatrix} y \\ -x \end{bmatrix} + \tilde{U_0} \begin{bmatrix} 1 \\ 0 \end{bmatrix} \tag{A.2}$$

Under the assumption of high tip-speed ratio ($\omega R >> U_0$) equation A.1 reduces to

$$\begin{bmatrix} U_x \\ U_y \end{bmatrix} = \omega cos(\eta) \begin{bmatrix} y \\ -x \end{bmatrix} + \omega R \begin{bmatrix} 1 \\ 0 \end{bmatrix}. \tag{A.3}$$

In this case, the similarity between the two motions is clear, with the equivalent pitch rate being equal to the orbital speed ($\tilde{\omega} = \omega cos(\eta)$) and the equivalent free stream velocity equal to the induced speed at the blade attachment point ($\tilde{U_0} = \omega R$).

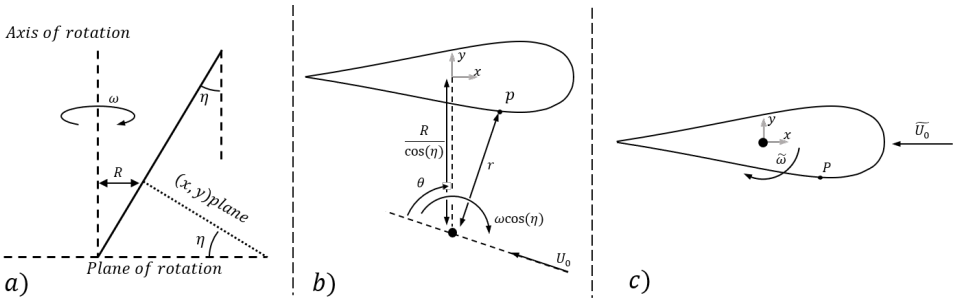

Figure A1. Similarity between the dynamics of a an aerofoil in orbital rotation and an aerofoil in a pitching motion.

Appendix A.2. Angle of attack Correction

An effective angle of attack correction can be obtained based on the quasi-static lift coefficient on a flat plate in a pitching motion given in it's general form by[20]

$$\alpha_{eff} = \alpha_G + \left[\frac{c}{2} \left(\frac{1}{2} - \xi \right) \frac{\dot{\alpha}}{U_0} \right], \tag{A.4}$$

substituting the effective pitch rate and effective freestream velocity we have

$$\alpha' = \alpha + cos(\eta) \left\{ \frac{1}{4} \frac{c}{R} + \frac{1}{2} \frac{(1 - 2\xi)c}{R} \right\}. \tag{A.5}$$

Appendix A.3. Conformal mapping

Beginning with the simplified form of the velocity given in equation A.3, we can obtain the stream function, ψ which describes the shape of the streamlines and is given by

$$d\psi = U_x dy - U_y dx \tag{A.6}$$

integration yields

$$\psi = \left(\frac{\omega}{2}cos(\eta)y + \omega R\right) y + \frac{\omega}{2}cos(\eta)x^2 + C \tag{A.7}$$

Where C represents an arbitrary constant of integration. This can be rearranged with constants absorbed into the constant of integration and with the potential appropriately scaled to give

$$\psi = \left[\frac{y}{R} + \frac{1}{cos(\eta)}\right]^2 + \left[\frac{x}{R}\right]^2. \tag{A.8}$$

For a new coordinate system given by

$$x' = \frac{x}{R} \text{ and } y' = \frac{y}{R} + \frac{1}{cos(\eta)} \tag{A.9}$$

The streamfunction is representative of streamlines that are concentric circles around the origin. In the complex plane, with $z = x' + iy'$, the circles are represented by

$$z = \sqrt{\psi}e^{i\theta} \text{ for } [0 \leq \theta < 2\pi] \tag{A.10}$$

the mapping function

$$g(z) = u + i\nu = i|z|(1 + ln(z)) \tag{A.11}$$

transforms the concentric circular streamlines into straight rectilinear flow. The conformal mapping process then simply involves the conversion of the aerofoil coordinates into the coordinate system described in equation A.9 then the application of the transform given in equation A.11, and the transformation back into the traditional aerofoil coordinate system. Figure A2 shows an example of this transform applied to a NACA0025 aerofoil with a chord to radius ratio of 0.2 for $\eta = 45°$, compared to the mapping process proposed by Migliore in [30]. In this case, the additional incidence angle from the Migliore transform is 2.8°, whilst the added incidence angle from the new transform is 2°.

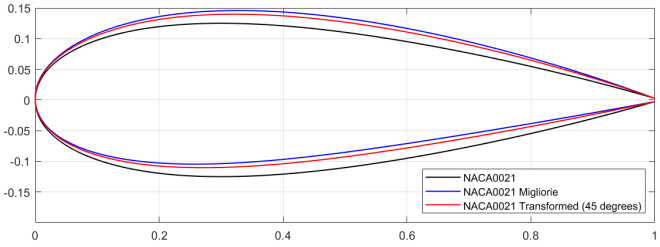

Figure A2. Demonstration of including the effects of the angle η on the conformal mapping process.